

# Automatic Segmentation of Retinal Layer in OCT Images With Choroidal Neovascularization

Dehui Xiang<sup>ID</sup>, Haihong Tian, Xiaoling Yang, Fei Shi<sup>ID</sup>, Weifang Zhu, Haoyu Chen, and Xinjian Chen

**Abstract**—Age-related macular degeneration is one of the main causes of blindness. However, the internal structures of retinas are complex and difficult to be recognized due to the occurrence of neovascularization. Traditional surface detection methods may fail in the layer segmentation. In this paper, a supervised method is reported for simultaneously segmenting layers and neovascularization. Three spatial features, seven gray-level-based features, and 14 layer-like features are extracted for the neural network classifier. The coarse surfaces of different optical coherence tomography (OCT) images can thus be found. To describe and enhance retinal layers with different thicknesses and abnormalities, multi-scale bright and dark layer detection filters are introduced. A constrained graph search algorithm is also proposed to accurately detect retinal surfaces. The weights of nodes in the graph are computed based on these layer-like responses. The proposed method was evaluated on 42 spectral-domain OCT images with age-related macular degeneration. The experimental results show that the proposed method outperforms state-of-the-art methods.

**Index Terms**—Choroidal neovascularization, optical coherence tomography, neural network and graph search.

## I. INTRODUCTION

AGE-RELATED macular degeneration (AMD) is one of the most leading causes of blindness particularly in people older than 60 years and leads to about 8% of all blindness worldwide [1]. Choroidal neovascularization is a typical feature of late-stage AMD and is mainly identified by the growth of abnormal blood vessels from the choroid through retinal pigment epithelium (RPE)/Bruch's complex with possible extension into the subretina [2]. There have been

Manuscript received May 5, 2017; revised October 28, 2017, January 16, 2018, and May 18, 2018; accepted July 12, 2018. Date of publication July 26, 2018; date of current version September 4, 2018. This work was supported in part by the National Basic Research Program of China (973 Program) under Grant 2014CB748600, in part by the National Natural Science Foundation of China (NSFC) under Grant 61401293, Grant 81371629, Grant 61401294, Grant 81401451, and Grant 81401472, and in part by the National Science Fund of Talented Young Scholars under Grant 61622114. The associate editor coordinating the review of this manuscript and approving it for publication was Prof. Oleg V. Michailovich. (Corresponding authors: Dehui Xiang; Xinjian Chen.)

D. Xiang, H. Tian, X. Yang, F. Shi, W. Zhu, and X. Chen are with the School of Electronic and Information Engineering, Soochow University, Suzhou 215006, China, and also with the State Key Laboratory of Radiation Medicine and Protection, School of Radiation Medicine and Protection, Soochow University, Suzhou 215006, China (e-mail: xiangdehui@suda.edu.cn; xjchen@suda.edu.cn).

H. Chen is with the Joint Shantou International Eye Center, Shantou University, Shantou, China, and also with the Chinese University of Hong Kong, Shantou 515041, China.

Color versions of one or more of the figures in this paper are available online at <http://ieeexplore.ieee.org>.

Digital Object Identifier 10.1109/TIP.2018.2860255

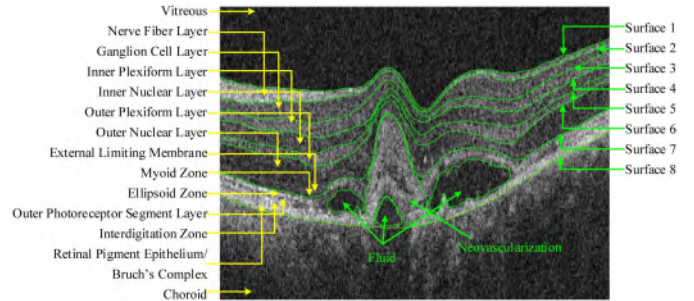


Fig. 1. An OCT image with neovascularization and manual annotations.

significant advances in the effective treatment of exudative or wet AMD with the introduction of anti-angiogenesis therapy, and these treatments can prevent blindness and even restore vision; however, they are expensive and therapeutic effect varies from different patients [1]. Thus, it is important to investigate and evaluate the treatment effects of anti-angiogenesis therapy for each patient and provide appropriate and adequate health care.

Optical coherence tomography (OCT) is a noninvasive and non-contact imaging modality for morphological analysis and diagnosis of retinal abnormality, such as AMD and glaucoma. The OCT images are often used to diagnose and monitor retinal diseases more accurately based on abnormality quantification and retinal layer thickness computation both in research centers and clinic routines [2]–[5]. Fig. 1 shows a macular centered OCT B-scan image with neovascularization. The vitreous, retina, neovascularization, fluid and choroid were annotated with arrows. The retinal structures are nerve fiber layer (NFL), ganglion cell layer (GCL), inner plexiform layer (IPL), inner nuclear layer (INL), outer plexiform layer (OPL), outer nuclear layer (ONL), external limiting membrane (ELM), myoid zone, ellipsoid zone, outer photoreceptor segment layer (OPSL), interdigitation zone, retinal pigment epithelium (RPE)/Bruch's complex, neovascularization, fluid and choroid. Surfaces are annotated and numbered 1 to 8 from top to bottom in this figure.

To quantify the thickness of retinal layers and volume of neovascularization, it is important to develop a reliable and automatic segmentation method for both retinal layers and neovascularization since manual segmentation is time-consuming for huge amount of OCT images in clinic applications. However, there are several challenges. First, internal

structures of retinas are complex and difficult to be recognized as shown in Fig. 1. Second, there may be abnormalities such as neovascularization and fluid. This leads to low contrast and blurred boundaries in OCT images between retinal layers, and also great structural changes of retinal layers. Layer segmentation may fail in using traditional surface detection methods such as traditional graph search algorithm [6], [7].

To overcome the problems presented above, we focus on segmentation of retinas with exudative AMD in OCT images, which is associated with neovascularization and possible fluid. An automatic, supervised 3-D layer segmentation method is proposed for macular-centered OCT images with exudative AMD. Shapes and intensities of retinal layers are learned by a neural network (NN) classifier. Layer-like responses are used to construct a graph for the graph search algorithm, which is constrained with the recognized initial surfaces. Compared to our previous work [7], it is much more difficult to detect surfaces in OCT images with AMD due to the complexity of neovascularization. The novelty of the proposed method lies in:

- 1) Multi-scale bright and dark layer-like structure detection filters are designed for estimation of possible bright and dark retinal layers with different thickness.
- 2) Twenty four features are introduced to the NN classifier aiming at finding the initial surfaces of retinal layers affected by neovascularization.
- 3) The weights of nodes in the graph are computed based on the original image and the layer structure detection responses, and then a constrained graph search algorithm is proposed to accurately detect surfaces between retinal layers even though OCT images with neovascularization are of low contrast and layer boundaries are blurred.
- 4) Layer segmentation and abnormal region segmentation are simultaneously performed and the proposed method achieves higher accuracy than previous graph search algorithms [6], [7].

## II. RELATED WORK

Many methods for retinal layer segmentation have been reported. These can be divided into two groups: rule-based methods and supervised methods. In the first group, the graph search algorithm is often used. In the second group, supervised methods are those based on voxel classification and then initial surface refinement is followed.

Regarding rule-based methods, layer segmentation methods attempt to obtain the initial surfaces of retinas and then detect the final surfaces. Many methods have been proposed for automatic retinal layer segmentation of OCT images of normal eyes [8]–[16]. These methods are mostly based on the graph search algorithm. The interfaces of vitreous-NFL and ellipsoid zone-OPSL were first obtained and then were used to constrain surface detection of the rest of interfaces. This is because these boundaries of vitreous-NFL and ellipsoid zone-OPSL are clear. Although authors claimed the method was based on the trained models, only hard and soft constraints were obtained for graph construction in [11] for normal eyes. In previous work, we proposed a multi-resolution graph search method to perform simultaneous layer segmentation and abnormal region

segmentation. This method was effective to OCT images with serous pigment epithelial detachment since subretinal layers is clearly visible [7]. Some other methods were also proposed. Novosel *et al.* [17] developed a loosely-coupled level sets method to simultaneously segment retinal layers coupling through the order of layers and thickness priors and eight interfaces were detected in the OCT images from normal eyes. Then, they developed a locally-adaptive loosely-coupled level sets method to simultaneously segment retinal layers and fluids in OCT images with central serous retinopathy [18].

On the other hand, supervised methods are based on voxel classification. Classifiers are trained by supervised learning with manually labeled images. Vermeer *et al.* [19] used support vector machines with features based on image intensities and gradients to detect five interfaces of retinas for both normal and glaucomatous eyes. Lang *et al.* [20] introduced a random forest classifier to segment eight retinal layers in macular cube images. The features were mainly designed for normal eyes for boundary classification with high contrast between neighboring layers. Xu *et al.* [21] developed a voxel classification based approach using a layer-dependent stratified sampling strategy to segment intraretinal and subretinal fluid. Hassan *et al.* [22] used a structure tensor approach combined with a nonlinear diffusion process for the automated detection of ELM and choroid in order to discriminate macular edema and central serous retinopathy from OCT images using a support vector machine classifier.

Recently, neural network classifiers were used for the segmentation in retinal images. Marín *et al.* [23] computed a 7-D vector composed of gray-level and moment invariants-based features and used neural networks for blood vessel detection in digital retinal images. Li *et al.* [24] used a deep neural network to segment vessels in retinal images. van Grinsven *et al.* [25] dynamically selected misclassified negative samples during training to speed-up deep learning network training in order to detect hemorrhages in color fundus images. However, these neural network classifiers were mainly used to segment vessels in color fundus images. Fang *et al.* [26] combined convolutional neural networks and a graph theory dynamic programming method to segment nine layer boundaries on OCT images with non-exudative AMD but without neovascularization and fluid. However, the features were extracted from a 2D sliding window; therefore, this method ignored the class labels' spatial structure. Roy *et al.* [27] used fully convolutional network to segment retinal layers and fluid in 2D OCT images with diabetic macular edema but without neovascularization. However, consecutive convolution layers are interleaved with spatial pooling operations, and can result in low resolution features. Many small structures such as thin layers may be lost, although subsequent upsampling operators and convolutions can be used to learn more precise output.

## III. METHOD

In this paper, a novel supervised segmentation framework is proposed to address the aforementioned challenges in the segmentation module of the retinal neovascularization treatment. As shown in Fig. 2, the proposed framework contains

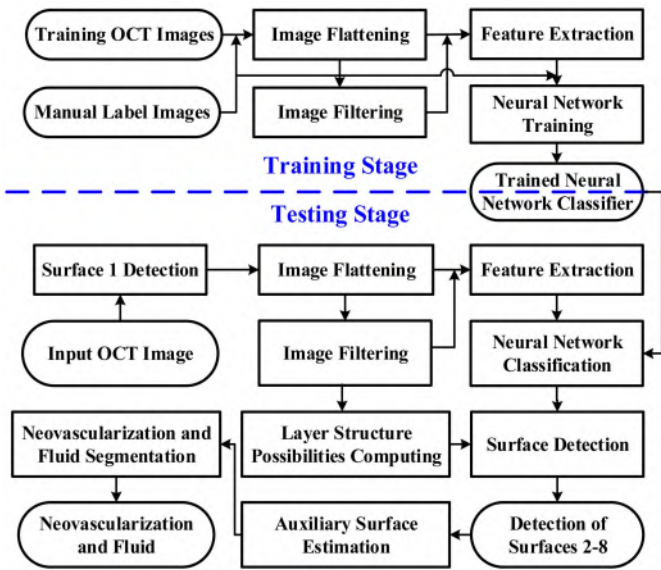


Fig. 2. The flowchart of the proposed framework. One typical OCT image in Fig. 1 undergoes each step in the testing stage of the framework, and the intermediate results are shown in Fig. 3 to Fig. 5.

two stages: training stage and testing stage. In the training stage, OCT images are manually annotated and features are extracted for the NN classifier training. In the testing stage, the proposed segmentation framework is a coarse-to-fine segmentation process that consists of three steps: preprocessing, initialization and segmentation. Original OCT image is pre-processed to reduce noise and gray levels are normalized. The necessary feature vector is computed from preprocessed OCT image and initial surfaces are computed with the application of the trained NN classifier to label voxels as different retinal layers. The final surfaces are refined via a layer constrained graph searching algorithm and neovascularization is also segmented.

### A. Preprocessing

To reduce the effect of the eye movement, image flattening is often employed to correct the irregular displacements [7], [9]. Surface 1 is the top interface between the vitreous and retina. In order to flatten a training or testing OCT image, Surface 1 needs to be detected. In training stage, the manually annotated image is scanned along A-line to find the interface between vitreous and NFL as Surface 1. In testing stage, initial Surface 1 is fast detected. First, noise smoothing is performed slice by slice by convolving B-scan images of the original 3D OCT image with a Gaussian kernel of dimensions  $l \times l = 9 \times 9$ , mean  $\mu = 0$  and standard variance  $\sigma = 1.0$ . Second, voxel intensities of the smoothed image are modified according to the following gray-level global transformation function:

$$I_N(\vec{x}) = \begin{cases} I_{N,\max}; & I_f(\vec{x}) \geq I_{f,s} + I_{f,r}; \\ \frac{I_{N,\max}}{I_{f,r}} (I_f(\vec{x}) - I_{f,s}); & I_{f,s} < I_f(\vec{x}) < I_{f,s} + I_{f,r}; \\ 0; & I_f(\vec{x}) \leq I_{f,s}. \end{cases} \quad (1)$$

where,  $\vec{x}$  denotes the voxel coordinates,  $I_N(\vec{x})$  is the normalized intensity of a voxel,  $I_f(\vec{x})$  is the intensity of a voxel in the smoothed image,  $I_{f,r}$  is the normalized range, the intensity interval is  $[I_{f,s}, I_{f,s} + I_{f,r}]$ ,  $I_{N,\max}$  is the maximal normalized intensity. In the experiments,  $I_{f,s}$  is calculated by the minimal value  $I_{f,\min}(\vec{x})$  and the maximal value  $I_{f,\max}(\vec{x})$  of the smoothed image, i.e.,  $I_{f,s} = I_{f,\min}(\vec{x}) + \tau_f (I_{f,\max}(\vec{x}) - I_{f,\min}(\vec{x}))$ ,  $\tau_f$  is set to 0.25, and  $I_{f,s} + I_{f,r}$  is set to the maximal value  $I_{f,\max}(\vec{x})$ .  $I_{N,\max}$  is set to 255. Canny edge detection algorithm is used to obtain initial Surface 1. The multi-resolution graph search algorithm [7] is used to detect Surface 1 according to initial Surface 1. In training and testing stage, voxels below Surface 1 in each A-line are top aligned to flatten images.

### B. Neural Network for Initial Surface Detection

Recently, supervised classification has been introduced into normal layer recognition of ophthalmic OCT images [19], [20]. Vermeer *et al.* [19] used the support vector machine classifiers to classify pixels. Lang *et al.* [20] used random forest classifier to segment eight retinal layers. Those two methods mainly used A-line or B-scan features to provide a probability of belonging to each layer; however, these methods did not consider characteristics of 3D retinal layers. In addition, due to the occurrence of the neovascularization, the boundaries between two layers are blurred and the OCT image is also of low contrast. Previous methods may fail in detecting retinal layer boundaries in the OCT images with retinal diseases. Therefore, we focus on describing and learning 3D retinal layers so that it is easier to find the initial layers in the OCT images with neovascularization.

1) *Feature Extraction:* A proper feature vector needs to be created for voxel characterization before the voxel is labeled by a set of classifiers. In terms of some quantifiable measurements, a voxel combined with its feature vector and label is used to train the multi-layer neurons, and the training algorithm iteratively adjusts the weights to enable the network to give the desired label to the provided feature vector. The voxel representation is also used in the classification stage to decide which retinal layer the voxel belongs to. In this paper, the following sets of features are selected in the training stage and testing stage.

- *Spatial Features:* three features based on voxel's coordinates for describing the distance to reference surface and its position in nasal/temporal side of the retina.
- *Gray Level based Features:* seven features based on non-enhanced and enhanced intensities of the voxel due to the difference of the intensity ranges between different layers.
- *Layer-like Features:* fourteen features based on layer shape responses for differentiating the darker layers and the brighter layers with different thickness.

a) *Spatial features:* Voxel's coordinates help to localize the voxel in a candidate layer using a coordinate system that is unified by a reference surface. However, fovea is often deformed by neovascularization, and it is difficult to locate

the center of the fovea by computing the thinnest position between the retinal boundaries as in [20]. After Surface 1 is detected, the depth (distance) to Surface 1 for each voxel in the flattened image can be calculated as  $z$  coordinate. The original  $x$  and  $y$  coordinates are also considered as features. These three features represent the geometric information.

*b) Gray level based features:* Since the dark layers and bright layers are always interleaved from top to bottom, features based on intensities can describe the difference of the intensity ranges between different layers. The image denoised with the curvature anisotropic diffusion filtering is considered as a feature. In the clinical images, the intensity range varies from one patient to another and the contrast between neighboring layers is often low due to the occurrence of neovascularization. To address these problems, the filtered and smoothed image are normalized in several intervals as Eq.(1).

*c) Layer-like features:* The layers in OCT images can be approximated by plate structures. These plate-like structures are not all equally thick and may be oriented at any angle. A selective layer detection filter can reduce responses from non-layer structures and enhance layer structures. Several papers have introduced techniques for structure extraction based on the eigen-decomposition of the Hessian computed at each image pixel/voxel, and typically reported in the application of vessel enhancement [28], [29]. Following this procedure for a given voxel at  $\vec{x} = (x, y, z)$  of a smoothed OCT image  $I_f(\vec{x})$ , Hessian matrix  $H(\vec{x}, \sigma_t)$  of the image in scale space is computed for the estimation of the possibility of a layer element in a 3D OCT image, where  $\sigma_t$  is variance of a Gaussian function. For bright layer structures,  $\lambda_3(\vec{x}, \sigma_t) < 0$  has to be satisfied; while for dark layer structures,  $\lambda_3(\vec{x}, \sigma_t) > 0$  has to be satisfied. The bright layer possibility is estimated in the scale space as

$$L(\vec{x}, \sigma_t) = \begin{cases} |\lambda_3(\vec{x}, \sigma_t)| \cdot \exp\left(-\frac{\alpha\lambda_1^2(\vec{x}, \sigma_t) + \beta\lambda_2^2(\vec{x}, \sigma_t)}{\lambda_3^2(\vec{x}, \sigma_t)}\right), & \lambda_3(\vec{x}, \sigma_t) < 0 \\ 0, & \lambda_3(\vec{x}, \sigma_t) \geq 0 \end{cases} \quad (2)$$

The dark layer possibility is defined as

$$L(\vec{x}, \sigma_t) = \begin{cases} |\lambda_3(\vec{x}, \sigma_t)| \cdot \exp\left(-\frac{\alpha\lambda_1^2(\vec{x}, \sigma_t) + \beta\lambda_2^2(\vec{x}, \sigma_t)}{\lambda_3^2(\vec{x}, \sigma_t)}\right), & \lambda_3(\vec{x}, \sigma_t) > 0 \\ 0, & \lambda_3(\vec{x}, \sigma_t) \leq 0 \end{cases} \quad (3)$$

where  $\alpha$  and  $\beta$  are symmetric parameters, which control the ratio between the two minor components  $\lambda_1(\vec{x}, \sigma_t)$ ,  $\lambda_2(\vec{x}, \sigma_t)$  to the principal component  $\lambda_3(\vec{x}, \sigma_t)$ .

To take into account the varying sizes of the layers, the scale-dependent layer possibility function  $L(\vec{x}, \sigma_t)$  is computed for varying thickness in the 3D image domain. The thickness values are discretized between the minimal scale  $\sigma_{t,min}$  and the maximal scale  $\sigma_{t,max}$ , using a linear scale. The multiscale layer response is obtained by selecting the

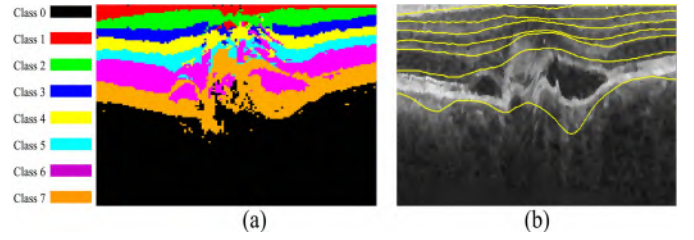


Fig. 3. Automatic initial surface detection. (a) Voxel classification via neural network prediction; (b) The seven initial curves/surfaces with the filtered image.

maximum response over the range of all scales as

$$L_m(\vec{x}, \sigma_t) = \max_{\sigma_{t,min} \leq \sigma_t \leq \sigma_{t,max}} L(\vec{x}, \sigma_t) \quad (4)$$

*2) Classification:* Two classification stages can be distinguished: a training stage, in which the NN configuration is chosen and the NN is trained, and a prediction stage, in which the trained NN is used to classify each voxel which layer belongs to.

*a) Neural network training:* The retinal layers in OCT images with neovascularization are manually labeled as eight classes. Class 1: NFL, Class 2: GCL, Class 3: IPL, Class 4: INL, Class 5: OPL, Class 6: ONL + ELM + myoid zone, Class 7: ellipsoid zone + OPSL + interdigitation zone + RPE/Bruch's complex + neovascularization + fluid, and Class 0: choroid. A multilayer feedforward network, consisting of an input layer, two hidden layers and an output layer, is used in this paper. The input layer consists of a number of neurons that equals to the dimension of the feature vector (24 neurons). The two hidden layers are both given 100 neurons. Since NN does not support categorical variables explicitly due to the logistic nonlinear sigmoidal activation function, an 8D binary vector of eight components is used instead of the output class label (one element for one class); therefore, the output layer contains eight neurons. The back-propagation algorithm is used to train the model.

*b) Neural network prediction:* At this stage, the trained NN is applied to an unseen OCT image to generate a label image. For each voxel under the surface vitreous-NFL, voxels' feature descriptions are individually passed through the trained NN. Due to the inability to handle categorical data, the trained NN gives a vector of probabilities to the unseen voxel at the prediction stage. The highest probability can be accepted as the winning class label output by the network. Fig. 3(a) shows the result of NN classification on one OCT image. As can be seen in Fig. 3(a), most voxels are given correct labels except a few voxels. The misclassification leads to inaccurate surface detection. To solve this problem, morphological opening and closing operations are employed for each class. Initial Surface 2 is first searched along A-line downwards. Initial Surface 3 is then searched along A-line downwards started from initial Surface 2. Initial Surfaces 4-7 are also detected as Surface 3. Initial Surface 8 is finally searched along A-line upwards. The initial curves/surfaces are smoothed by computing the average  $z$  value in  $x$  and  $y$  directions, as shown in Fig. 3(b).

### C. Constrained Graph Search for Surface Detection

The graph search algorithm is used to refine positions of the vertices in the initial surfaces. Compared to the previous work by [7]–[9], [11], [15], and [30], a new cost function is formulated based on layer structure detection, allowing detection of the optimal surfaces of retinal layers even though the contrast between neighboring layers is low and morphological changes of retinal layers are large due to neovascularization and fluid.

As developed in the LOGISMOS framework by [8] and [31], optimal surface detection can be transformed into finding a minimum-cost closed set in a corresponding vertex-weighted graph. Briefly, this involves two important tasks. First, Surfaces 2-6 were detected by the constraints of Surface 7 in previous work [7]–[9], [11], [15], [30]; however, due to neovascularization and fluid, the boundaries of myoid zone and ellipsoid zone in OCT images are not clear as those of normal layers and greatly deformed, leading to Surfaces 2-7 not being accurately detected by complying with previous procedures. Although shape and context priors were learned in [11], only smoothness constraints were obtained to constrain the neighboring nodes. That is why the initial surfaces are found via the NN classification. Second, the proper formulation of a cost function should be provided since it measures the possibility that each node in the graph belongs to a particular surface, and determines the optimal surface with the lowest cost. Therefore, a proper initialization of surfaces and an improved cost function help to detect surfaces more accurately in OCT images with diseases than previous methods.

A weighted and directed graph  $G$  [6], [7] is constructed in a narrowband around each initial surface. Each node in  $G$  corresponds to a voxel in the subvolume of images. Nodes in graph  $G$  are connected with three types of weighted and directed arcs: the intra-column arc  $E^{\text{intra}}$ , the inter-column arc  $E^{\text{inter}}$ , and the terminal arc  $E^{\text{terminal}}$ . The intra-column arc  $E^{\text{intra}}$  connects two neighboring nodes in a column. The inter-column arc  $E^{\text{inter}}$  connects two neighboring nodes in two neighboring columns. The terminal arc  $E^{\text{terminal}}$  connects nodes in  $G$  to two terminal nodes  $S$  or  $T$ , if the weight is positive then the node is connected to the terminal node  $S$ ; otherwise, the node is connected to the terminal node  $T$ . For the  $(x, y)$ th column in a graph, a node can be denoted as  $V(x, y, v)$  for the graph  $G$  ( $v = 1, 2, \dots, N_u + N_b + 1$ ). In the application,  $N_u$  and  $N_b$  are set to the same number for all the initial surfaces. The node in the neighboring  $(x', y')$ th column can be denoted as  $V(x', y', v)$ . Mathematically, the three types of arcs can be written as,

$$E^{\text{intra}} = \langle V(x, y, v), V(x, y, v - 1) \rangle, \quad v > 1, \quad (5)$$

$$E^{\text{inter}} = \langle V(x, y, v), V(x', y', v - u) \rangle, \quad v > u, u > 0, \quad (6)$$

$$E^{\text{terminal}} = \begin{cases} \langle S, V(x, y, v) \rangle, & \omega(V(x, y, v)) > 0; \\ \langle V(x, y, v), T \rangle, & \omega(V(x, y, v)) \leq 0; \end{cases} \quad (7)$$

where  $u$  is the inter-column smoothness constraint for the outer or inner surface.  $\omega$  is the weight of a node  $V(x, y, v)$ .

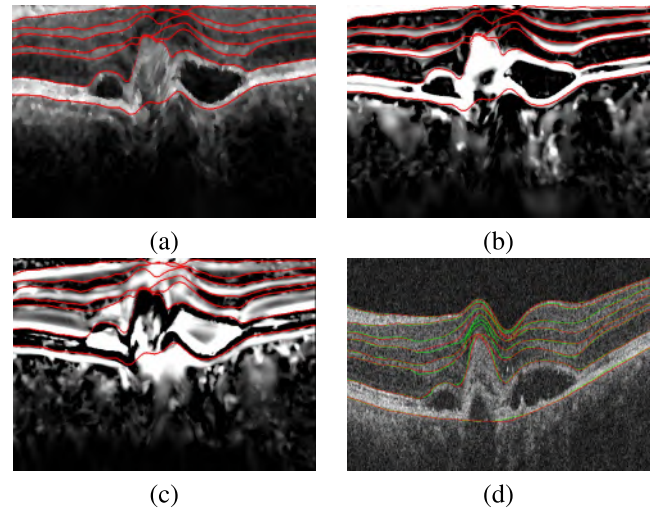


Fig. 4. Automatic surface detection. (a) The curvature anisotropic diffusion filtered image and the detected surfaces (red curves) via the constrained graph search algorithm; (b) The bright layer possibility image and the detected surfaces (red curves) via the constrained graph search algorithm; (c) The dark layer possibility image and the detected surfaces (red curves) via the constrained graph search algorithm; (d) Final surfaces (red curves) via the constrained graph search algorithm, manual annotated surfaces (blue curves) and a B-scan image of the original OCT image.

For the first two types of arcs  $E^{\text{intra}}$  and  $E^{\text{inter}}$ , the cost is set to infinity. The cost of terminal arcs can be defined as the absolute value of the weight of the corresponding node. The weight of a node for an initial surface is defined as

$$\omega(V(x, y, v)) = \begin{cases} -B(V(x, y, v)) \\ +B(V(x, y, v - 1)), & v > 1; \\ -B(V(x, y, v)), & v = 1; \end{cases} \quad (8)$$

where  $B(V(x, y, v))$  is the edge-related cost function for each node in the graph  $G$ . There are two types of edge-related cost functions: dark-to-bright for Surfaces 1, 3, 5, 7 and bright-to-dark for Surfaces 2, 4, 6, 8. The Sobel operator is used to compute the gradient magnitude of the boundary cost image in  $z$ -direction in order to assign the edge-related cost for each node. The boundary cost image is defined according to the filtered image and the layer enhanced images, including the bright layer possibility image computed as Eq. (2) as shown in Fig. 4(b) and the dark layer possibility image computed as Eq. (3) as shown in Fig. 4(c). With the constraints of layer structure possibilities, the boundary cost image integrates three types of boundary cost associated with the three images: the filtered image  $I_f(x, y, v)$ , the bright layer possibility image  $L_b(x, y, v, \sigma_t)$  and the dark layer possibility image  $L_d(x, y, v, \sigma_t)$ . The total voxel cost of the boundary cost image can be written as the weighted sum of the three images as given below:

$$C(x, y, v) = \varpi I_f(x, y, v) + \theta L_b(x, y, v, \sigma_t) - \vartheta L_d(x, y, v, \sigma_t), \quad (9)$$

where  $\varpi$ ,  $\theta$ ,  $\vartheta$  are three weighted parameters. The three images  $I_f(x, y, v)$ ,  $L_b(x, y, v, \sigma_t)$  and  $L_d(x, y, v, \sigma_t)$  are normalized to  $[0, 255]$  computed as Eq. (1) before the total

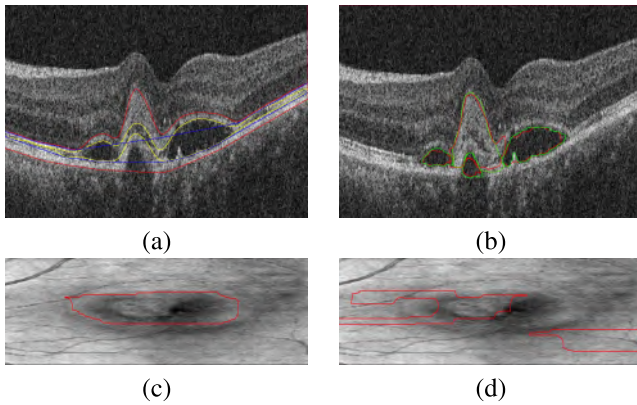


Fig. 5. Automatic surface detection. (a) The yellow curves are Surface 7b and Surface 8t, the blue curves are the bottom contours of Surface 7b and Surface 8t; (b) The red curves are the segmented neovascularization and fluid and the green curves are the manual annotated neovascularization and fluid; (c) The red curve is the footprint of abnormal regions below Surface 7; (d) The red curve is the footprint of abnormal regions below Surface 8t.

voxel cost  $C(x, y, v)$  is calculated. Since NN classifiers can compute class probability for each layer, class probability from adjacent layers can be also used to constrain the graph search algorithm as Eq.(9). Since most surfaces in OCT images are corrupted with speckles, the interfaces and the boundaries of the retinal layers except that between vitreous and NFL are blurred and of low contrast. Surface detection errors may be produced without strong constraints of layer boundaries. Therefore, the initial surfaces and the hybrid boundary cost functions are proposed to detect surfaces of retinal layers affected by neovascularization and fluid.

#### D. Neovascularization Segmentation

The layers under Surface 7 often locally are deformed upwards around neovascularization. Fluid caused by neovascularization often occurs. To detect neovascularization and fluid, positions need to be estimated. This is done by computing the height of the deformed surfaces and the occurrence of fluid.

Surface 7 changes abruptly and is deformed in the abnormal region while its original pre-disease position used to be a smooth surface. For each curve of Surface 7 in each B-scan, the corresponding bottom contour is computed via the convex hull algorithm [32]. The footprints of the deformed Surface 7 can be found by scanning each curve of Surface 7 and its bottom contour in each B-scan. The pixel is considered in the footprints of the abnormal region if the distance between Surface 7 and its bottom contour is larger than a threshold value (twenty-voxel height). Neovascularization and fluid are then segmented constrained by the footprint of the abnormal region.

Two auxiliary surfaces (Surface 7b and Surface 8t) are also estimated between these two surfaces via the constrained graph search algorithm as shown in Fig. 5(a). Surface 7b (the top yellow curve in Fig. 5(a)) is detected according to the bright-to-dark edge-related cost function, and then Surface 8t (the bottom yellow curve in Fig. 5(a)) is detected between Surface 7b and Surface 8 according to the dark-to-bright edge-related cost function. Fluid is segmented via thresholding constrained between Surface 7 and Surface 8. The voxel is

considered to be in neovascularization region via thresholding between Surface 7 and Surface 8t. The voxels are excluded between Surface 7 and Surface 8t if the height between Surface 7 and Surface 8t is smaller than mean thickness of the normal region. The voxel is also considered to be in neovascularization region if the height between Surface 8t and Surface 8 is larger than mean thickness in the normal region. The bottom contour of Surface 8 is also computed via the convex hull algorithm [32]. Neovascularization and fluid are segmented via thresholding between Surface 8 and the bottom contour of Surface 8.

#### IV. EXPERIMENTAL EVALUATION

The OCT images were obtained from the Joint Shantou International Eye Center by using a Cirrus HD-OCT 4000 machine. Macula-centered 42 SD-OCT scans with AMD were acquired as testing images. Another 6 macula-centered SD-OCT images with AMD were used as training images. The OCT volume images contain  $512 \times 128 \times 1024$  voxels with voxel size of  $11.74 \times 47.24 \times 1.96 \mu m^3$ .

To evaluate the layer segmentation results, retinal specialists manually annotated the surfaces in the B-scan images to form the segmentation reference. Due to the time consumption of manual annotation, only 10 out of the 128 B-scans were randomly chosen and annotated for each 3D OCT volume in the testing data set. All the 128 B-scans were manually annotated for each 3D OCT volume in the training data set, and then each 3D OCT volume was labeled with the eight classes according to the annotated surfaces for the NN classifier training. To evaluate the neovascularization segmentation results, neovascularization were also manually annotated for each 3D OCT volume in the testing data set. All the 128 B-scan images were scanned slice by slice for manual neovascularization segmentation. This study was approved by the intuitional review board of Joint Shantou International Eye Center and adhered to the tenets of the Declaration of Helsinki.

To evaluate performance of surface detection methods, average unsigned surface detection error (AUSDE) was computed for each surface by measuring absolute Euclidean distance in the z-axis between surface detection results of the algorithms and the reference standard, average signed surface detection error (ASSDE) was computed for each surface by measuring distance in the z-axis between surface detection results of the algorithms and the reference standard [7]. To evaluate performance of neovascularization segmentation methods, we used three measures: true positive fraction (TPF), false positive fraction (FPF) and Dice similarity coefficient (DSC) [7]. To demonstrate the improvement of our method, the NN + constrained graph search algorithm (NNCGS) was compared with the state-of-art methods: the Iowa reference algorithm (IR) [6], the multi-resolution graph search algorithm (MGS) [7], the NN + multi-resolution graph search algorithm (NNMGS), the support vector machine + constrained graph search algorithm (SVMCGS) and the random forest + constrained graph search algorithm (RFCGS). Paired t-tests were used to compare surface detection and fluid segmentation errors and a p-value less than 0.05 was considered statistically significant.

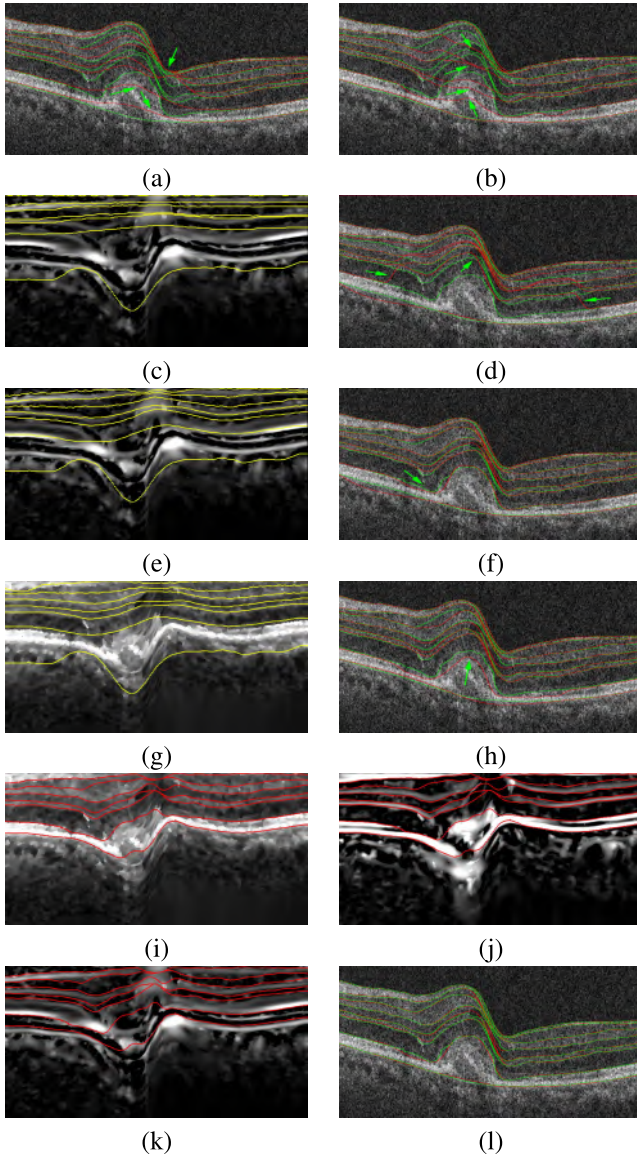


Fig. 6. Automatic surface detection (green curves are the segmentation reference, red curves are detected surfaces) of an OCT image with neovascularization. (a) Surfaces were detected via the IF algorithm; (b) Surfaces were detected via the MGS algorithm; (c) The seven initial surfaces via the SVM classification; (d) Surfaces were detected via the SVMCGS algorithm; (e) The seven initial surfaces via the RF classification; (f) Surfaces were detected via the RFCGS algorithm; (g) The seven initial surfaces via the NN classification; (h) Surfaces were detected via the NNMGS algorithm; (i) Surfaces were detected via the NNCGS algorithm with the flattened and filtered image; (j) Surfaces were detected via the NNCGS algorithm with the flattened bright layer response image ( $\sigma_{t,\min} = 1.0, \sigma_{t,\max} = 4.0$ ); (k) Surfaces were detected via the NNCGS algorithm with the flattened dark layer response image ( $\sigma_{t,\min} = 1.0, \sigma_{t,\max} = 4.0$ ); (l) Final surfaces were detected via the NNCGS algorithm.

## V. EXPERIMENTAL RESULTS

### A. Surface Detection Results

An OCT volume image is only with neovascularization as shown in Fig. 6. Another OCT image is with neovascularization and fluid as shown in Fig. 7. The green curves are manual annotated surfaces. The red curves are the detected surfaces via the surface detection algorithms. The yellow curves are the seven initial surfaces by using classifiers. Table I shows the mean and standard deviation of unsigned surface detection

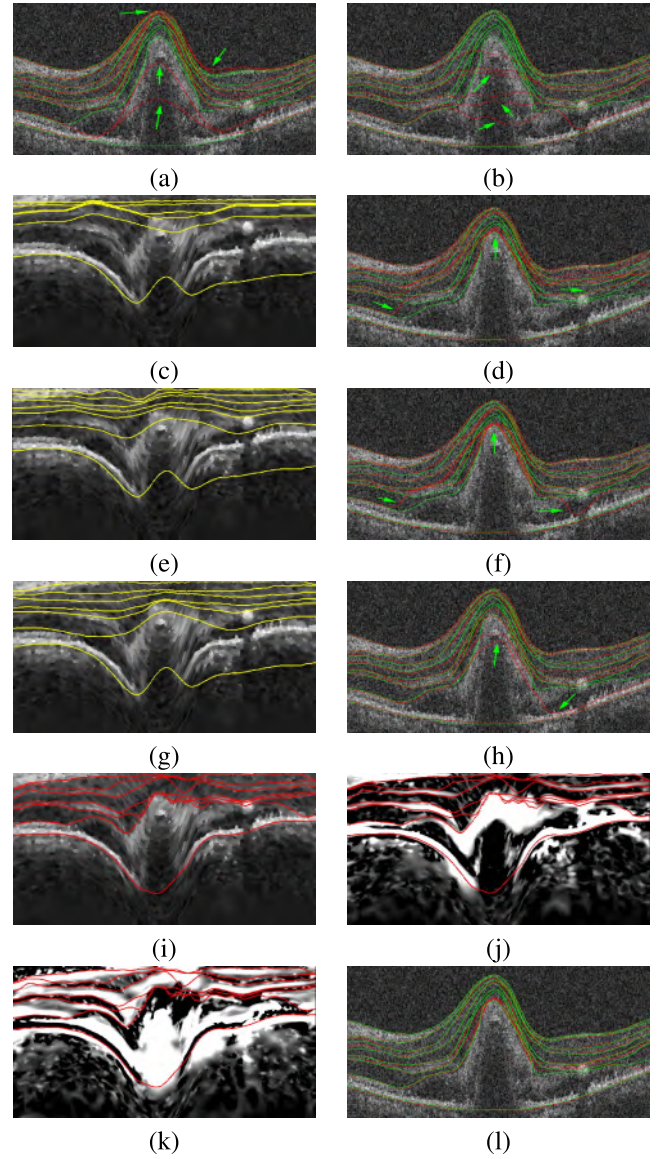


Fig. 7. Automatic surface detection (green curves are the segmentation reference, red curves are detected surfaces) of an OCT image with neovascularization and fluid. (a) Surfaces were detected via the IF algorithm; (b) Surfaces were detected via the MGS algorithm; (c) The seven initial surfaces via the SVM classification; (d) Surfaces were detected via the SVMCGS algorithm; (e) The seven initial surfaces via the RF classification; (f) Surfaces were detected via the RFCGS algorithm; (g) The seven initial surfaces via the NN classification; (h) Surfaces were detected via the NNMGS algorithm; (i) Surfaces were detected via the NNCGS algorithm with the flattened and filtered image; (j) Surfaces were detected via the NNCGS algorithm with the flattened bright layer response image ( $\sigma_{t,\min} = 1.0, \sigma_{t,\max} = 4.0$ ); (k) Surfaces were detected via the NNCGS algorithm with the flattened dark layer response image ( $\sigma_{t,\min} = 1.0, \sigma_{t,\max} = 4.0$ ); (l) Final surfaces were detected via the NNCGS algorithm.

error. The p-values of AUSDE are shown in Table II. Table III shows the mean and standard deviation of signed surface detection error. The p-values of ASSDE for each surface are shown in Table IV.

For the IR algorithm [6], AUSDEs of Surface 1-8 were obviously large as shown in the first column of Table I, and surface detection errors were the largest at Surface 8 while detection errors of the rest surfaces were slightly smaller. These surface detection errors were consistent with surface

TABLE I  
COMPARISON OF SURFACE DETECTION WITH AVERAGE UNSIGNED SURFACE DETECTION ERROR (MEAN±SD  $\mu\text{m}$  §)

Surface	IR	MGS	NNMGS	SVMCGS	RFCGS	NNCGS
1	2.48 ± 1.01	2.43 ± 1.29	0.81 ± 0.14	0.81 ± 0.14	0.81 ± 0.14	0.81 ± 0.14
2	5.97 ± 2.72	7.31 ± 6.24	2.37 ± 0.42	4.22 ± 3.51	2.92 ± 0.86	2.36 ± 0.41
3	9.06 ± 6.13	13.77 ± 10.10	4.67 ± 1.83	16.02 ± 5.58	5.17 ± 2.56	2.51 ± 1.01
4	6.84 ± 5.57	10.39 ± 8.48	6.90 ± 5.53	14.64 ± 9.32	3.70 ± 4.41	2.28 ± 1.15
5	8.30 ± 6.93	15.19 ± 14.69	6.76 ± 5.22	27.4 ± 19.19	6.03 ± 8.98	3.13 ± 3.09
6	8.76 ± 8.05	15.70 ± 15.62	7.16 ± 5.43	32.1 ± 21.65	8.40 ± 10.15	4.81 ± 3.92
7	16.26 ± 23.48	13.95 ± 16.27	11.37 ± 6.77	30.49 ± 28.21	6.74 ± 7.46	3.34 ± 3.64
8	13.27 ± 12.63	7.36 ± 5.21	10.22 ± 9.39	8.67 ± 10.40	8.38 ± 10.71	8.23 ± 10.53

§ Voxel size in z direction is 1.96 $\mu\text{m}$ .

TABLE II  
P-VALUES OF AVERAGE UNSIGNED SURFACE DETECTION ERROR

Surface	NNCGS vs IR	NNCGS vs MGS	NNCGS vs SVMCGS	NNCGS vs RFCGS	NNCGS vs NNMGS
1	$5.91 \times 10^{-14}$	$3.59 \times 10^{-10}$			
2	$2.13 \times 10^{-10}$	$8.90 \times 10^{-6}$	$6.13 \times 10^{-4}$	$1.60 \times 10^{-6}$	0.34
3	$4.23 \times 10^{-8}$	$1.34 \times 10^{-8}$	$6.26 \times 10^{-18}$	$1.48 \times 10^{-8}$	$1.39 \times 10^{-9}$
4	$9.80 \times 10^{-7}$	$1.77 \times 10^{-7}$	$3.79 \times 10^{-10}$	0.04	$2.22 \times 10^{-6}$
5	$6.75 \times 10^{-8}$	$2.40 \times 10^{-7}$	$4.04 \times 10^{-10}$	0.04	$3.52 \times 10^{-8}$
6	$9.91 \times 10^{-5}$	$4.23 \times 10^{-6}$	$9.29 \times 10^{-11}$	0.02	$5.74 \times 10^{-4}$
7	$6.27 \times 10^{-4}$	$6.69 \times 10^{-5}$	$2.00 \times 10^{-7}$	$2.60 \times 10^{-3}$	$4.82 \times 10^{-10}$
8	0.03	0.49	0.02	0.50	$2.91 \times 10^{-5}$

TABLE III  
COMPARISON OF SURFACE DETECTION WITH AVERAGE SIGNED SURFACE DETECTION ERROR (MEAN±SD  $\mu\text{m}$  §)

Surface	IR	MGS	NNMGS	SVMCGS	RFCGS	NNCGS
1	0.66 ± 0.63	-0.27 ± 0.69	-0.11 ± 0.15	-0.11 ± 0.15	-0.11 ± 0.15	-0.11 ± 0.15
2	-0.86 ± 3.6	3.25 ± 6.81	-1.37 ± 1.09	-3.21 ± 4.00	-1.17 ± 1.76	-1.38 ± 1.09
3	3.22 ± 6.49	7.93 ± 10.50	-1.16 ± 2.26	-15.01 ± 6.34	-1.98 ± 3.54	1.10 ± 1.32
4	-0.27 ± 5.68	1.78 ± 9.33	5.35 ± 6.07	-13.85 ± 9.69	-1.70 ± 4.88	-0.48 ± 1.30
5	-1.24 ± 7.14	5.96 ± 14.95	4.98 ± 5.35	-26.41 ± 19.62	-2.41 ± 9.39	0.91 ± 3.27
6	0.41 ± 7.80	5.67 ± 15.49	2.82 ± 5.70	-31.37 ± 22.07	-4.94 ± 10.03	-1.08 ± 4.22
7	9.87 ± 25.61	9.18 ± 17.92	10.11 ± 6.92	-28.11 ± 29.43	-0.75 ± 8.46	2.69 ± 4.05
8	-9.54 ± 12.11	-1.92 ± 5.03	2.77 ± 12.35	6.02 ± 11.77	5.58 ± 11.93	5.75 ± 11.81

§ Voxel size in z direction is 1.96 $\mu\text{m}$ .

TABLE IV  
P-VALUES OF AVERAGE SIGNED SURFACE DETECTION ERROR

Surface	NNCGS vs IR	NNCGS vs MGS	NNCGS vs SVMCGS	NNCGS vs RFCGS	NNCGS vs NNMGS
1	$1.04 \times 10^{-9}$	0.11			
2	0.28	$1.70 \times 10^{-5}$	$9.64 \times 10^{-4}$	0.09	0.47
3	0.06	$2.81 \times 10^{-4}$	$2.37 \times 10^{-20}$	$1.64 \times 10^{-7}$	$1.54 \times 10^{-6}$
4	0.81	0.10	$5.54 \times 10^{-11}$	0.10	$5.70 \times 10^{-8}$
5	0.01	0.01	$7.98 \times 10^{-11}$	0.02	$9.17 \times 10^{-10}$
6	0.17	$4.19 \times 10^{-3}$	$2.91 \times 10^{-11}$	0.01	$3.06 \times 10^{-6}$
7	0.06	0.02	$5.49 \times 10^{-8}$	$6.76 \times 10^{-3}$	$1.92 \times 10^{-8}$
8	$1.48 \times 10^{-8}$	$8.34 \times 10^{-6}$	0.12	0.56	$8.51 \times 10^{-7}$

detection results shown in Fig. 6(b) and Fig. 7(b). Surface detection error occurred at Surface 7 and Surface 8 where the large neovascularization made layers to be deformed upwards.

For the MGS algorithm [7], AUSDEs of Surfaces 7, 8 were slightly smaller than those of the IR algorithm while AUSDEs of Surfaces 2-6 were larger than those of the IR algorithm as shown in the second column of Table I. As shown in Fig. 6(c) and Fig. 7(c), surface detection error occurred from Surfaces 2-8 also due to the appearance of the neovascularization. The surface detection via the MGS algorithm for OCT images with neovascularization first segmented Surface 7 and then Surfaces 2-6 were refined with Surface 7; therefore, Surfaces 2-6 tended to be detected incorrectly as Surface 7 and the mean surface detection errors of Surfaces 5-7 were large as shown in Fig. 6(c) and Fig. 7(c).

The results in the third column of Table I show AUSDEs of Surfaces 1-8 except Surface 4 were smaller than those of

the IR algorithm. Compared to the MGS algorithm, AUSDEs of Surfaces 1-7 were smaller while AUSDE of Surface 8 was slightly larger via the NNMGS algorithm. Due to initialization via NN classification, most surfaces were detected more accurately than the method without initialization. The reason of inaccurate detection of Surface 8 is that Surface 8 was detected in a subvolume via the NNMGS algorithm while the Surface 8 was detected in the whole volume.

The results of SVMCGS were shown in the 4th column of Table I. AUSDEs of Surfaces 1, 2, 8 were smaller than those of the IR algorithm. AUSDEs of Surfaces 1, 2 were smaller than those of the MGS algorithm. AUSDE of Surface 8 was smaller than those of the NNMGS algorithm. AUSDEs of Surfaces 3-7 were the largest, compared to the rest of the algorithms. The results of RFCGS were shown in the 5th column of Table I. AUSDEs of all surfaces were smaller than those of the IR algorithm. AUSDEs of Surfaces 3-7 were smaller than those

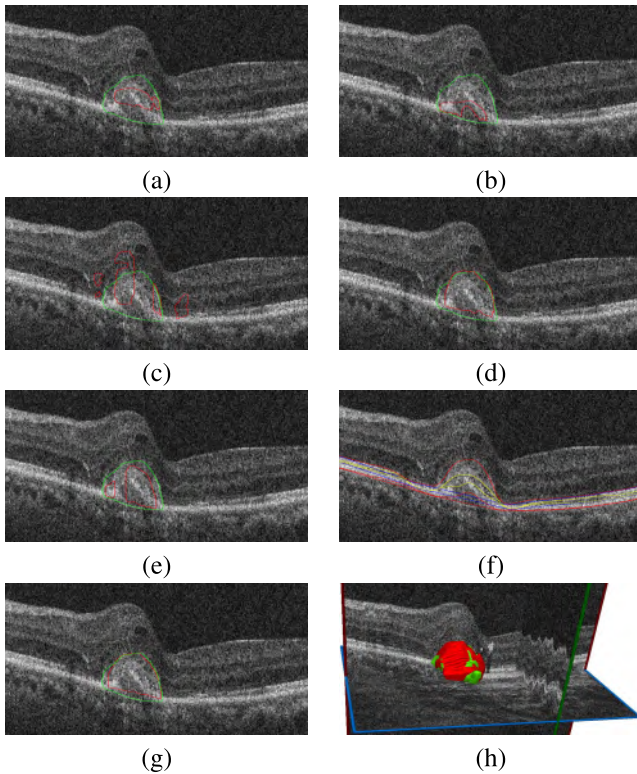


Fig. 8. Automatic neovascularization segmentation (green curves are the segmentation reference, red curves are segmented neovascularization) of an OCT image with neovascularization. (a) Neovascularization was segmented via the IF algorithm; (b) Neovascularization was segmented via the MGS algorithm; (c) Neovascularization was segmented via the SVMCGS algorithm; (d) Neovascularization was segmented via the RFCGS algorithm; (e) Neovascularization was segmented via the NNMGS algorithm; (f) Auxiliary surfaces for neovascularization segmentation via the NNCGS algorithm (yellow curves are Surface 7b and Surface 8t, blue curves are the bottom contours of Surface 7 and Surface 8t, red curves are segmented surfaces); (g) Neovascularization was segmented via the NNCGS algorithm; (h) 3D visualization of neovascularization segmented via the NNCGS algorithm (red) and manual annotation (green).

of the MGS algorithm. AUSDEs of Surfaces 2-8 were smaller than those of the SVMCGS algorithm.

Table I shows the proposed method has a great improvement over the IR algorithm and the MGS algorithm even a large proportion of the layers exhibits dramatic morphological changes. As can be seen in Table II, AUSDEs of Surfaces 1-8 of the NNCGS algorithm were significantly smaller than those of the IR algorithm. AUSDEs of Surfaces 1-7 of the NNCGS algorithm were significantly smaller than those of the MGS algorithm. AUSDEs of Surface 8 was not significantly different between the MGS algorithm and the NNCGS algorithm. As can be seen in Fig. 6(b)(c) and Fig. 7(b)(c), Surfaces 2-7 were detected via the IR algorithm and the MGS algorithm lower than reference surfaces. As can be seen in the first and second columns of Table III, ASSDEs of Surfaces 2-7 were mostly positive. It means the mean position of the detected Surfaces 2-7 via the IR algorithm and the MGS algorithm were lower than that of the segmentation reference. This is due to low intensity of the layers above the abnormal region and large morphological changes of the layers.

Compared to the SVMCGS algorithm, AUSDEs of Surfaces 2-8 were significantly reduced via the NNCGS

algorithm as shown in Table I and Table II ( $p < 0.05$ ). The absolute ASSDEs of Surfaces 2-8 were also significantly reduced as shown in Table III and Table II ( $p < 0.05$ ). As can be seen in the 4th column of Table III, ASSDEs of Surfaces 1-7 were negative. It means the average positions of the detected Surfaces 1-7 via the SVMCGS algorithm were higher than that of the segmentation reference, which is consistent with Fig. 6(e) and Fig. 7(e). Compared to the RFCGS algorithm, AUSDEs of Surfaces 2-7 via the NNCGS algorithm were smaller and significantly different as shown in Table I and Table II ( $p < 0.05$ ). AUSDE of Surface 8 was statistically indistinguishable between the RFCGS algorithm and the NNCGS algorithm as shown in Table II ( $p \geq 0.05$ ). Compared to the RFCGS algorithm, ASSDEs of Surfaces 2, 3, 5, 6, 7 via the NNCGS algorithm were smaller and significantly different as shown in Table III and Table IV ( $p < 0.05$ ). As can be seen in the 5th column of Table III, ASSDEs of Surface 1-7 were negative. It means the average positions of the detected Surfaces 1-7 via the RFCGS algorithm were higher than that of the segmentation reference, which is consistent with Fig. 6(g) and Fig. 7(g). AUSDEs of Surfaces 4, 8 were statistically indistinguishable between the RFCGS algorithm and the NNCGS algorithm as shown in Table IV ( $p \geq 0.05$ ).

Compared to the NNMGS algorithm, AUSDEs of Surfaces 1-8 were also reduced via the NNCGS algorithm as shown in the fourth column of Table I. As can be seen in the third column of Table III, ASSDEs of Surfaces 4-8 were positive. It means the average position of the detected Surfaces 4-8 via the NNMGS algorithm were lower than that of the segmentation reference. For Surface 7, the occurrence of neovascularization lead to large morphological changes of the layers as shown in Fig. 1, Fig. 6 and Fig. 7. As can be seen in Fig. 6(d) and Fig. 7(d), the detected Surface 7 dropped under the segmentation reference. However, the ellipsoid zone was higher enhanced via the bright layer detection filter while it was much weak for the bright layer responses of the ELM layer as shown in Fig. 6(g) and Fig. 7(g) with a large scale. Compared to the NNMGS algorithm, the NNCGS algorithm improved the detection of Surface 7 as shown in Fig. 6(i) and Fig. 7(i). As can be seen in Table II, AUSDEs of Surfaces 3-8 of the NNCGS algorithm were significantly smaller than those of the NNMGS algorithm ( $p < 0.05$ ). AUSDE of Surface 2 was not significantly different between the NNMGS algorithm and NNCGS algorithm.

### B. Neovascularization Segmentation Results

An example of neovascularization segmentation result of an OCT image only with neovascularization is shown in Fig. 8 and also another example with neovascularization and fluid is shown in Fig. 9. The green curves are manually annotated neovascularization and fluid. The red curves are the segmented neovascularization via the neovascularization segmentation algorithms. Table V shows the mean and standard deviation of TPF, FPF and DSC. The p-values of the three evaluation measures of neovascularization segmentation are shown in Table VI. The fluid segmentation was not evaluated since many OCT images were not with fluid.

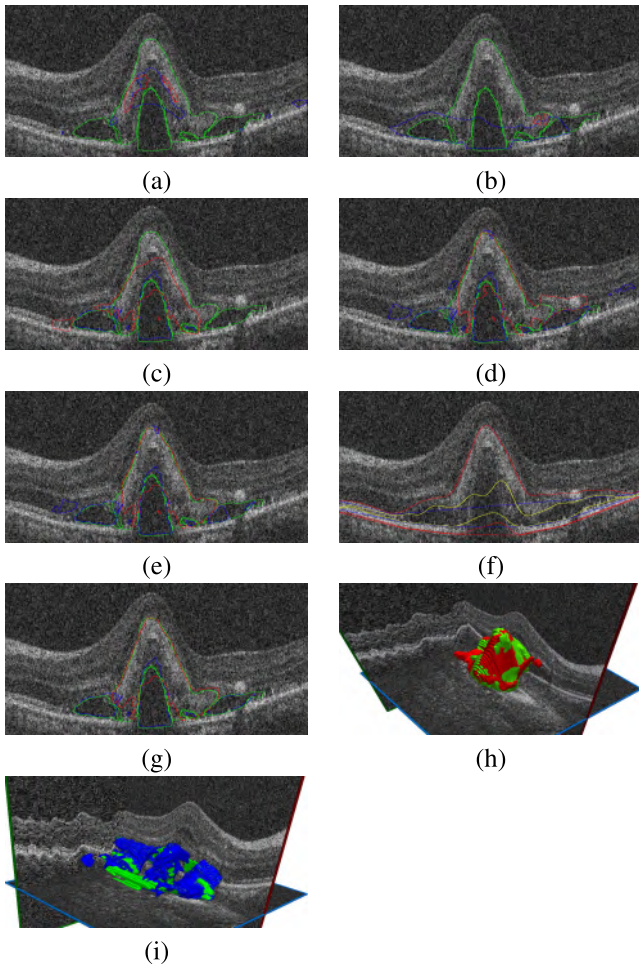


Fig. 9. Automatic neovascularization and fluid segmentation (green curves are the segmentation reference, red curves are segmented neovascularization, blue curves are segmented fluid) of an OCT image with neovascularization and fluid. (a) Neovascularization and fluid were segmented via the IF algorithm; (b) Neovascularization and fluid were segmented via the MGS algorithm; (c) Neovascularization and fluid were segmented via the SVMCGS algorithm; (d) Neovascularization and fluid were segmented via the RFCGS algorithm; (e) Neovascularization was segmented via the NNMGS algorithm; (f) Auxiliary surfaces for neovascularization segmentation via the NNCGS algorithm (yellow curves are Surface 7b and Surface 8t, blue curves are the bottom contours of Surface 7 and Surface 8t, red curves are segmented surfaces); (g) Neovascularization and fluid were segmented via the NNCGS algorithm; (h) 3D visualization of neovascularization segmented via the NNCGS algorithm (red) and manual annotation (green); (i) 3D visualization of fluid segmented via the NNCGS algorithm (blue) and manual annotation (green).

For the IR algorithm [6] and the MGS algorithm [7], the same method was employed to segment neovascularization on the same dataset. The neovascularization was segmented between Surface 7 and Surface 8 detected. Because of the inaccurate surface detection, small region of neovascularization was obtained as shown in Fig. 8(a) and Fig. 9(a). This led to much lower values of TPF, FPF and DSC as shown in the first row of Table V. The IR algorithm [6] and the MGS algorithm [7] were not robust to deformation of retinal layers, and thus a little improvement was achieved as shown in the second row of Table V. For the NNMGS, SVMCGS and RFCGS algorithms, the same method was also used to segment neovascularization on the same dataset between Surface 7 and Surface 8. This is also because the NNMGS

TABLE V  
COMPARISON OF NEOVASCULARIZATION SEGMENTATION (MEAN±SD %)

	TPF	FPF	DSC
IR	8.02 ± 9.61	0.002 ± 0.01	13.37 ± 15.36
MGS	32.22 ± 27.97	0.04 ± 0.07	36.81 ± 30.07
NNMGS	50.77 ± 25.79	0.11 ± 0.20	54.49 ± 22.17
SVMCGS	70.15 ± 21.25	0.67 ± 0.48	41.10 ± 21.41
RFCGS	79.73 ± 12.53	0.15 ± 0.17	75.15 ± 10.27
NNCGS	82.12 ± 11.70	0.05 ± 0.08	84.54 ± 9.53

TABLE VI  
P-VALUES OF NEOVASCULARIZATION SEGMENTATION

NNCGS vs	TPF	FPF	DSC
IR	$3.12 \times 10^{-34}$	$3.47 \times 10^{-4}$	$5.64 \times 10^{-29}$
MGS	$4.84 \times 10^{-12}$	0.56	$1.32 \times 10^{-11}$
NNMGS	$5.36 \times 10^{-11}$	0.06	$2.51 \times 10^{-11}$
SVMCGS	$1.55 \times 10^{-4}$	$2.76 \times 10^{-10}$	$2.41 \times 10^{-16}$
RFCGS	0.11	$3.94 \times 10^{-5}$	$8.83 \times 10^{-10}$

algorithm produced large surface detection error of Surface 7. Compared to the NNMGS algorithm, TPF achieved to  $70.15 \pm 21.25\%$  via the SVMCGS algorithm, and TPF achieved to  $79.73 \pm 12.53\%$  via the RFCGS algorithm; however, FPF reached  $0.67 \pm 0.48\%$  and  $0.15 \pm 0.17\%$ , respectively. DSC was  $75.15 \pm 10.27\%$  via the RFCGS algorithm. TPF achieved to  $82.12 \pm 11.70\%$  via the NNCGS algorithm, DSC achieved to  $84.54 \pm 9.53\%$  and FPF reduced to  $0.05 \pm 0.08\%$ . As shown Table VI, most index values of the NNCGS algorithm were statistically different from those of the IR algorithm, the MGS algorithm, the NNMGS algorithm, the SVMCGS algorithm and the RFCGS algorithm.

## VI. CONCLUSION AND FUTURE WORK

In this paper, a supervised method is proposed for the automatic segmentation of retinal layers on SD-OCT scans of eyes with neovascularization. After Surface 1 is detected by using the Canny edge detection algorithm and multi-resolution graph search algorithm, the B-scan image is aligned and flattened. Only twenty four features are generated for the training and testing of the NN classifier, and then seven initial surfaces are detected for the accurate surface detection. By utilizing the original intensities of OCT images and the layer-like shape information, a modified graph is constructed to refine surfaces. Surfaces between neighboring layers are successively detected from Surfaces 2-8 based on the constrained graph search algorithm. With the proper surface detection, neovascularization segmentation can be segmented by using a thresholding method. The proposed method can also cope with the OCT images with neovascularization and fluid.

The surface detection errors were statistically significantly smaller than errors obtained from employing the state-of-art methods such as the IR algorithm [6] and the MGS algorithm [7] because of the occurrence of neovascularization and fluid. Meanwhile, the NNCGS algorithm also outperformed the NNMGS algorithm. This is because the ellipsoid zone was higher enhanced via the bright layer detection filter while the ELM layer was restrained. Simultaneous neovascularization and fluid segmentation were also achieved. The proposed method also achieved higher true positive fraction and Dice similarity coefficient, which were statistically different from

the results obtained by the IR algorithm [6], the MGS algorithm [7] and the NNMGS algorithm. As for voxel classification of the OCT images with neovascularization and fluid, NN classifiers outperform SVM classifiers and RF classifiers.

There are several limitations in our work. Surfaces detection accuracy is limited in layers where the contrast between layers is low and their boundaries are not visible due to the occurrence of neovascularization. As can be seen in Fig. 4(d), Fig. 6(i) and Fig. 7(i), the detected boundaries above neovascularization were not close to reference boundaries, although these boundaries were tried to be refined again after the initial boundaries were refined via the constrained graph search algorithm. Indeed, most inadequate results above neovascularization are due to the disappearance of the layers and the reference boundaries are estimated by retinal specialists. As can be seen in Table I and Table III, both AUSDE and ASSDE of Surface 8 were larger than the rest of surfaces. Because of neovascularization in choroid, the intensities under Surface 8 are much higher than usual and the contrast between choroid and RPE is significantly reduced. Therefore, the detected boundaries are lower than the reference boundaries and ASSDE of Surface 8 is positive and large. Further work can also include the segmentation of choroid neovascularization before Surface 8 is detected. Recently, deep neural networks have achieved great success in image segmentation tasks. In the future, the proposed hand-crafted features will be combined with learned deep convolutional features to capture image context information and improve segmentation accuracy.

Another limitation of this work is its high computing time requirement. The algorithms were implemented in C++ and tested on a PC with Intel i5-3450 CPU@3.10GHz and 16GB of RAM. The average running time of the IF algorithm is  $97 \pm 32$ s for surface detection. The average running time of the MGS algorithm was  $266 \pm 116$ s for surface detection. The average running time of the NNMGS algorithm was  $286 \pm 123$ s for surface detection. The average running time of the SVMCGS algorithm was  $742 \pm 148$ s for surface detection. The average running time of the RFCGS algorithm was  $688 \pm 104$ s for surface detection. The average running time of the NNCGS algorithm was  $398 \pm 216$ s for surface detection. There are two key steps for reduction of running time. First, the bright layer possibility and the dark layer possibility were computed serially from small scale to large scale. Second, the max-flow/min-cut algorithm was also implemented for the CPU process. The long processing time may be reduced by parallelizing our method on graphic processing unit. The average running time of neovascularization and fluid was about  $335 \pm 145$ s. The bottom contours of Surface 7, Surface 8t and Surface 8 were estimated for each B-scan image. The convex hull algorithm is used only in the abnormal region and then the running time will be reduced. In addition, neovascularization and fluid were refined by morphological opening and closing in the whole image after the thresholding method which takes a long time. In the future, the abnormal region segmentation method will be used in the local region and faster and more accurate results will be obtained.

In the feature extraction stage, different hand-crafted features were introduced. In our implementation, we constrained ourselves into a neural network implementation without the use of extensive hardware support. Nowadays deep neural networks achieved great success in image recognition tasks. In the future, we will extend our work to new/different CNN architectures and their optimization for OCT images. Meanwhile, with the proper GPU supports, different successful architectures can be designed to handle hierarchical feature extraction at the different level of hierarchy and details. Available CNN architectures for OCT image analysis still use 2D images or 3D small patches to regularize the extreme need of memory issue, which puts a high-burden in computational design. Like many other hand-craft feature extraction models [19], [20], CNN is not at the desired level of success for capturing image features at the varying scales [33]. This is especially true when medical imagery is considered [34]–[37]. ResNET [34] and DenseNET [35] were all implemented with feature integration module at different level of hierarchy in the deep nets and the main reason is to enhance feature learning due to loss of details, as also clearly mentioned in these seminal works [35], [38]. Sabour *et al.* [33] released “CapsuleNET” architecture to solve the problem of scale-invariance feature learning. While CapsuleNET is a good attempt to explain different scale features, it is also just a beginning of new era in affine-invariance feature learning with deep nets.

Therefore, we summarize potential suggestions for the deep net architecture for learning more effective features from OCT images. 1) segmentation tasks should use encoder-decoder based neural network architecture designs such as U-Net [39], or modified DenseNET [35]. 2) Due to the requirement of large data for supervising the deep nets, there should be either transfer learning and fine-tuning of the network, or a data augmentation step and properly trained network from scratch. 3) Regularization of the network is quite an important field for a successful image analysis framework with deep nets. Therefore, dropout mechanisms with adaptive optimization algorithms (such as ADAM instead of pure SGD) should be used. 4) Network should include more average pooling than max pooling because segmentation tasks require mixed level of features for designing pixel level classification unlike max pooling where larger regions are better fit for classification purpose. 5) Skip connections, dense connections, or similar feature concatenation algorithms help to improve segmentations because features from small scales can be lost. Feature integration help to retain such properties. ResNET, DenseNET, or CapsuleNET kind of implementations are desirable.

#### ACKNOWLEDGEMENTS

The authors thank to Prof. Ulas Bagci in Center for Research in Computer Vision, University of Central Florida for the great help to suggest potential future work in deep net and polish English expressions in the manuscript.

#### REFERENCES

- [1] W. L. Wong *et al.*, “Global prevalence of age-related macular degeneration and disease burden projection for 2020 and 2040: A systematic review and meta-analysis,” *Lancet Global Health*, vol. 2, no. 2, pp. e106–e116, 2014.

- [2] Q. Zhang *et al.*, “Automated quantitation of choroidal neovascularization: A comparison study between spectral-domain and swept-source OCT angiograms,” *Invest. Ophthalmol. Vis. Sci.*, vol. 58, no. 3, pp. 1506–1513, 2017.
- [3] X. Chen *et al.*, “Quantification of external limiting membrane disruption caused by diabetic macular edema from SD-OCT,” *Invest. Ophthalmol. Vis. Sci.*, vol. 53, no. 13, pp. 8042–8048, 2012.
- [4] H. Chen, H. Xia, Z. Qiu, W. Chen, and X. Chen, “Correlation of optical intensity on optical coherence tomography and visual outcome in central retinal artery occlusion,” *Retina*, vol. 36, no. 10, pp. 1964–1970, 2016.
- [5] E. Gao *et al.*, “Comparison of retinal thickness measurements between the topcon algorithm and a graph-based algorithm in normal and glaucoma eyes,” *PLoS ONE*, vol. 10, no. 6, p. e0128925, 2015.
- [6] M. K. Garvin, M. D. Abramoff, X. Wu, S. R. Russell, T. L. Burns, and M. Sonka, “Automated 3-D intraretinal layer segmentation of macular spectral-domain optical coherence tomography images,” *IEEE Trans. Med. Imag.*, vol. 28, no. 9, pp. 1436–1447, Sep. 2009.
- [7] F. Shi *et al.*, “Automated 3-D retinal layer segmentation of macular optical coherence tomography images with serous pigment epithelial detachments,” *IEEE Trans. Med. Imag.*, vol. 34, no. 2, pp. 441–452, Feb. 2015.
- [8] M. K. Garvin, M. D. Abramoff, R. Kardon, S. R. Russell, X. Wu, and M. Sonka, “Intraretinal layer segmentation of macular optical coherence tomography images using optimal 3-D graph search,” *IEEE Trans. Med. Imag.*, vol. 27, no. 10, pp. 1495–1505, Oct. 2008.
- [9] M. K. Garvin, M. D. Abramoff, X. Wu, S. R. Russell, T. L. Burns, and M. Sonka, “Automated 3-D intraretinal layer segmentation of macular spectral-domain optical coherence tomography images,” *IEEE Trans. Med. Imag.*, vol. 28, no. 9, pp. 1436–1447, Sep. 2009.
- [10] S. Lu, C. Y.-L. Cheung, J. Liu, J. H. Lim, C. K.-S. Leung, and T. Y. Wong, “Automated layer segmentation of optical coherence tomography images,” *IEEE Trans. Biomed. Eng.*, vol. 57, no. 10, pp. 2605–2608, Oct. 2010.
- [11] Q. Song, J. Bai, M. K. Garvin, M. Sonka, J. M. Buatti, and X. Wu, “Optimal multiple surface segmentation with shape and context priors,” *IEEE Trans. Med. Imag.*, vol. 32, no. 2, pp. 376–386, Feb. 2013.
- [12] P. A. Dufour *et al.*, “Graph-based multi-surface segmentation of OCT data using trained hard and soft constraints,” *IEEE Trans. Med. Imag.*, vol. 32, no. 3, pp. 531–543, Mar. 2013.
- [13] Q. Yang *et al.*, “Automated layer segmentation of macular OCT images using dual-scale gradient information,” *Opt. Express*, vol. 18, no. 20, pp. 21293–21307, 2010.
- [14] D. Xiang *et al.*, “CorteXpert: A model-based method for automatic renal cortex segmentation,” *Med. Image Anal.*, vol. 42, pp. 257–273, Dec. 2017.
- [15] R. Kafieh, H. Rabbani, M. D. Abramoff, and M. Sonka, “Intra-retinal layer segmentation of 3D optical coherence tomography using coarse grained diffusion map,” *Med. Image Anal.*, vol. 17, no. 8, pp. 907–928, Dec. 2013.
- [16] D. Xiang *et al.*, “Automatic retinal layer segmentation of OCT images with central serous retinopathy,” *IEEE J. Biomed. Health Inform.*, p. 1, Feb. 2018.
- [17] J. Novosel, G. Thepass, H. G. Lemij, J. F. de Boer, K. A. Vermeer, and L. J. van Vliet, “Loosely coupled level sets for simultaneous 3D retinal layer segmentation in optical coherence tomography,” *Med. Image Anal.*, vol. 26, no. 1, pp. 146–158, Dec. 2015.
- [18] J. Novosel, Z. Wang, H. de Jong, M. van Velthoven, K. A. Vermeer, and L. J. van Vliet, “Locally-adaptive loosely-coupled level sets for retinal layer and fluid segmentation in subjects with central serous retinopathy,” in *Proc. IEEE 13th Int. Symp. Biomed. Imag. (ISBI)*, Apr. 2016, pp. 702–705.
- [19] K. A. Vermeer, J. van der Schoot, H. G. Lemij, and J. F. de Boer, “Automated segmentation by pixel classification of retinal layers in ophthalmic OCT images,” *Biomed. Opt. Express*, vol. 2, no. 6, pp. 1743–1756, 2011.
- [20] A. Lang *et al.*, “Retinal layer segmentation of macular OCT images using boundary classification,” *Biomed. Opt. Express*, vol. 4, no. 7, pp. 1133–1152, 2013.
- [21] X. Xu, K. Lee, L. Zhang, M. Sonka, and M. D. Abramoff, “Stratified sampling Voxel classification for segmentation of intraretinal and sub-retinal fluid in longitudinal clinical OCT data,” *IEEE Trans. Med. Imag.*, vol. 34, no. 7, pp. 1616–1623, Jul. 2015.
- [22] B. Hassan, G. Raja, T. Hassan, and M. U. Akram, “Structure tensor based automated detection of macular edema and central serous retinopathy using optical coherence tomography images,” *J. Opt. Soc. Amer. A, Opt. Image Sci.*, vol. 33, no. 4, pp. 455–463, 2016.
- [23] D. Marín, A. Aquino, M. E. Gegúndez-Arias, and J. M. Bravo, “A new supervised method for blood vessel segmentation in retinal images by using gray-level and moment invariants-based features,” *IEEE Trans. Med. Imag.*, vol. 30, no. 1, pp. 146–158, Jan. 2011.
- [24] Q. Li, B. Feng, L. Xie, P. Liang, H. Zhang, and T. Wang, “A cross-modality learning approach for vessel segmentation in retinal images,” *IEEE Trans. Med. Imag.*, vol. 35, no. 1, pp. 109–118, Jan. 2016.
- [25] M. J. van Grinsven, B. van Ginneken, C. B. Hoyng, T. Theelen, and C. I. Sánchez, “Fast convolutional neural network training using selective data sampling: Application to hemorrhage detection in color fundus images,” *IEEE Trans. Med. Imag.*, vol. 35, no. 5, pp. 1273–1284, May 2016.
- [26] L. Fang, D. Cunefare, C. Wang, R. H. Guymer, S. Li, and S. Farsiu, “Automatic segmentation of nine retinal layer boundaries in OCT images of non-exudative AMD patients using deep learning and graph search,” *Biomed. Opt. Express*, vol. 8, no. 5, pp. 2732–2744, 2017.
- [27] A. G. Roy *et al.* (2017). “ReLayNet: Retinal layer and fluid segmentation of macular optical coherence tomography using fully convolutional network.” [Online]. Available: <https://arxiv.org/abs/1704.02161>
- [28] A. F. Frangi, W. J. Niessen, K. L. Vincken, and M. A. Viergever, “Multiscale vessel enhancement filtering,” in *Proc. Int. Conf. Med. Image Comput. Comput.-Assist. Intervent.* Berlin, Germany: Springer, 1998, pp. 130–137.
- [29] R. Manniesing, M. A. Viergever, and W. J. Niessen, “Vessel enhancing diffusion: A scale space representation of vessel structures,” *Med. Image Anal.*, vol. 10, no. 6, pp. 815–825, 2006.
- [30] J. Tian, X. Wu, D. Z. Chen, and M. Sonka, “Optimal surface segmentation in volumetric images—A graph-theoretic approach,” *IEEE Trans. Pattern Anal. Mach. Intell.*, vol. 28, no. 1, pp. 119–134, Jan. 2006.
- [31] R. L. Graham and F. F. Yao, “Finding the convex hull of a simple polygon,” *J. Algorithms*, vol. 4, no. 4, pp. 324–331, 1983.
- [32] S. Sabour, N. Frosst, and G. E. Hinton, “Dynamic routing between capsules,” in *Proc. 31st Conf. Neural Inf. Process. Syst. (NIPS)*, Long Beach, CA, USA, vol. abs/1710.09829, Oct. 2017.
- [33] K. He, X. Zhang, S. Ren, and J. Sun, “Deep residual learning for image recognition,” in *Proc. IEEE Conf. Comput. Vis. Pattern Recognit. (CVPR)*, Las Vegas, NV, USA, 2016, pp. 770–778.
- [34] G. Huang, Z. Liu, L. van der Maaten, and K. Q. Weinberger, “Densely connected convolutional networks,” in *Proc. IEEE Conf. Comput. Vis. Pattern Recognit. (CVPR)*, Honolulu, HI, USA, 2017, pp. 2261–2269.
- [35] I. J. Goodfellow *et al.*, “Generative adversarial networks,” in *Machine Learning*. Neural Information Processing Systems Foundation, Inc., 2014.
- [36] A. Mortazi, R. Karim, K. S. Rhode, J. Burt, and U. Bagci, “CardiacNET: Segmentation of left atrium and proximal pulmonary veins from MRI using multi-view CNN,” in *Medical Image Computing and Computer-Assisted Intervention—MICCAI*. Cham, Switzerland: Springer, 2017, pp. 377–385.
- [37] K. He, X. Zhang, S. Ren, and J. Sun, “Deep residual learning for image recognition,” in *Proc. Comput. Vis. Pattern Recognit.*, Jun. 2016, pp. 770–778.
- [38] D. Morley, H. Foroosh, S. Shaikh, and U. Bagci, “Simultaneous detection and quantification of retinal fluid with deep learning,” *CoRR*, vol. abs/1708.05464, Aug. 2017.

**Dehui Xiang**, photograph and biography not available at the time of publication.

**Haihong Tian**, photograph and biography not available at the time of publication.

**Xiaoling Yang**, photograph and biography not available at the time of publication.

**Fei Shi**, photograph and biography not available at the time of publication.

**Weifang Zhu**, photograph and biography not available at the time of publication.

**Haoyu Chen**, photograph and biography not available at the time of publication.

**Xinjian Chen**, photograph and biography not available at the time of publication.